3-D convection with variable viscosity

U. Christensen and H. Harder
Max-Planck-Institut für Chemie, Saarstrasse 23, 6500 Mainz, FR Germany

SUMMARY

We report numerical calculations for 3-D convection with variable viscosity. A hybrid spectral and finite difference method is used. The coupling of modes in the equation of motion, which is caused by lateral viscosity variations, is treated iteratively. Solutions for bimodal, hexagonal, square, triangular and spoke patterns are reported for bottom heated convection at infinite Prandtl number. The Rayleigh number, based on the viscosity at the mean of top and bottom temperature, is between critical and 10^5, and temperature-induced viscosity contrasts up to 100 are considered (1000 in one case). In agreement with results from laboratory experiments we find that at low Rayleigh number temperature-dependent viscosity favours flow patterns like squares or hexagons, where a columnar rising current is surrounded by sheet-like descending flow. The dichotomy in geometry between upwelling and sinking flow becomes more pronounced with increasing viscosity contrast. The temperature dependence of viscosity gives rise to a toroidal velocity component; however, it amounts only to a few per cent of the total velocity. In contrast, at the earth's surface an approximate equipartitioning of poloidal and toroidal energy is found. We show that with non-Newtonian and depth-dependent rheology the toroidal component at the free surface can become significant, and a pattern reminiscent of plate motion can arise in a free convection model. Although these results are obtained in a parameter range which is not directly applicable to the earth, they support the conclusions that (i) upwelling flow in the mantle is unlikely to be sheet-like and will probably be in the form of columnar plumes, and that (ii) the toroidal motion found at the earth's surface is due to the highly non-linear rheology which leads to the existence of mobile surface plates and is not caused by viscosity variations related to lateral temperature contrasts deeper in the mantle.

Key words: convection, flow patterns, viscosity.

1 INTRODUCTION

Creep experiments on minerals at high temperature indicate that the viscosity of the mantle of the earth and other solid planets must be strongly dependent on temperature, pressure, and probably also on strain rate, i.e., the rheology is non-Newtonian (Kirby & Kronenberg 1987). The variability of viscosity plays an important role in the theory of mantle convection. For example, it causes the upper thermal boundary layer of convection to move as a nearly rigid but mobile plate. The consequences of variable viscosity for the flow pattern or the heat transport have been studied in various 2-D numerical model calculations (Turcotte, Torrance & Hsui 1973; Parmentier, Turcotte & Torrance 1976; Christensen 1984a, b, 1985; and many others). 2-D models are useful to determine at least qualitatively many of the properties of thermal convection under conditions relevant for the earth's mantle, but evidently 3-D studies are needed to resolve the planform and full geometry of the flow pattern.

When the viscosity is constant, 2-D (roll-like) convection becomes unstable at a Rayleigh number of 22 600 when the top and bottom boundaries are rigid and a bimodal flow pattern emerges, with weaker cross-rolls of shorter wavelength superimposed at right angle onto the primary rolls (Busse 1967; Frick, Busse & Clever 1983). At higher Rayleigh number ($>10^5$) more irregular and weakly time-dependent 'spoke'-patterns are found in laboratory experiments (Whitehead & Parsons 1978). If the symmetry of the flow is broken, for example when one boundary is rigid and the other stress-free, square or hexagonal patterns can be found at moderate Rayleigh number, where

sheet-like down- or upwelling surrounds jet- or plume-like up (down) flow (Cserepes, Rabinowicz & Rosenberg-Borot 1988). 3-D model calculations for convection in a spherical shell (Bercovici *et al.* 1989a, b) exhibit sheet-like downwelling flow, and, when at least part of the heat enters through the bottom, plume-like upwelling. Houseman (1988) obtained a similar result also for Cartesian geometry in partly bottom-heated cases. Even when plate-like movement is imposed at the surface, a preference for columnar upwelling and sheet-like downwelling is found (Cserepes & Christensen, 1990), especially in the presence of a low-viscosity layer near the surface.

This difference in the geometry of up- and downwelling flow agrees with the scanty evidence that we have on the structure of mantle convection. Descending lithospheric slabs seem to maintain a planar structure to the maximum depth to which they can be observed. The only positive evidence for active upwelling comes from hotspots, which are commonly interpreted to be caused by cylindrical mantle plumes. Mid-ocean ridges are thought to be 'passive' and surficial features and not connected to hot rising sheets coming from deep in the mantle. Although columnar upwelling can be found in constant viscosity convection under a variety of conditions, these columns are still fairly wide features. In contrast, mantle plumes are thought to be narrow conduits of very rapid flow (e.g., Loper & Stacey 1983) because of the strong decrease of viscosity with temperature. Thus, although temperature dependence of viscosity seems not to be a necessary condition for the formation of columnar upwelling, it may play an important role for determining the width and velocity of plumes.

White (1988) has performed a careful and extensive laboratory study on the various planforms of convection for variable viscosity convection. He found that for viscosity ratios exceeding approximately 10 and for Rayleigh numbers between critical and 2×10^4, only squares and hexagons (and perhaps triangles) are stable patterns with a columnar upwelling in the centre and sinking sheets at the sides of the geometrical figure. To our knowledge, the only theoretical work on finite-amplitude 3-D convection with variable viscosity is by Busse & Frick (1985), who also showed for small Rayleigh number (<5000) and moderate viscosity contrasts that squares become a stable form.

Any 3-D velocity field can be split into a poloidal part, for which the vertical vorticity is zero, and a toroidal part, which has zero vertical velocity. At the earth's surface, the toroidal component is manifest in the existence of transform faults, and the poloidal component in the presence of convergence and divergence, i.e. spreading and subduction zones. Analysing the motion of the plates, about equal energy is found in the toroidal and in the poloidal parts of the surface velocity (Hager & O'Connell 1979; Forte & Peltier 1987). However, for free convection at infinite Prandtl number in a fluid of constant viscosity or depth-dependent viscosity the toroidal component is identically zero. The only mechanism to excite toroidal flow is by lateral variations of viscosity due to temperature, composition or stress dependence, or other non-linearity of the rheology. Therefore convection models assuming constant Newtonian viscosity are unable to reproduce an important part of the circulation pattern found at the earth's surface. Ricard & Vigny (1989) showed that by introducing

internally rigid but mobile surface plates, which are coupled to the underlying buoyancy-driven flow in the mantle by balancing the torque between plate and mantle flow, a toroidal component of the correct order is obtained in the surface velocity field. However, their model made no direct reference to the kind of rheology which might produce surface plates.

In this work we describe numerical calculations of 3-D convection with variable viscosity for Rayleigh numbers up to 10^5. The viscosity contrast is up to one hundred in most cases, and in one example the contrast is increased to 1000. Our emphasis is put on evaluating the extent to which variable viscosity favours flow pattern exhibiting plume-like upwelling and sheet-like downwelling and on the amount and distribution of toroidal motion. In the following section the constitutive equations and the numerical method are treated. We present results for constant viscosity, temperature-dependent viscosity, and finally for strain-rate dependent rheology. Inferences for convection in the mantle of the earth are discussed in the concluding section.

2 CONSTITUTIVE EQUATIONS AND NUMERICAL METHOD

Thermal convection in a plane layer of fluid with an infinite Prandtl number is studied using the Boussinesq approximation. Top and bottom boundaries are kept at fixed temperatures. In most cases internal heat sources are not considered. All material properties are assumed to be constant, except for the (effective) viscosity, which may depend on temperature, depth, and in some cases on the strain rate. Using non-dimensional variables (see Table 1 for notation and the non-dimensionalization scheme) the problem is governed by the following equations:

$$\nabla \cdot \mathbf{u} = 0, \tag{1}$$

$$-\nabla p + \nabla : \tau_{ij} = Ra T \mathbf{e}_z, \tag{2}$$

$$\tau_{ij} = \eta \dot{\varepsilon}_{ij}, \tag{3}$$

$$\dot{\varepsilon}_{ij} = (\partial_j u_i + \partial_i u_j), \tag{4}$$

$$\partial_t T + \mathbf{u} \cdot \nabla T = \nabla^2 T + Q, \tag{5}$$

$$\eta = f(z, T, \dot{\varepsilon}), \tag{6}$$

together with appropriate boundary conditions. The number of unknowns is reduced by introducing the poloidal potential ϕ and the toroidal potential ψ (e.g. Busse & Frick 1985), from which the velocity is obtained as

$$\mathbf{u} = \nabla \times [\nabla \times (\phi \mathbf{e}_z)] + \nabla \times (\psi \mathbf{e}_z) \tag{7}$$

or

$$u = \partial_{xz}\phi + \partial_y\psi, \tag{7a}$$

$$v = \partial_{yz}\phi - \partial_x\psi, \tag{7b}$$

$$w = -(\partial_{xx} + \partial_{yy})\phi = -\Delta_2\phi, \tag{7c}$$

and the strain rate components are (operators F, G, Δ_2 defined in Table 1)

$$\dot{\varepsilon}_{xx} = 2(\partial_{xxz}\phi + \partial_{xy}\psi), \tag{8a}$$

$$\dot{\varepsilon}_{yy} = 2(\partial_{yyz}\phi - \partial_{xy}\psi), \tag{8b}$$

$$\dot{\varepsilon}_{zz} = -2\partial_z\Delta_2\phi, \tag{8c}$$

Table 1. Notation and scaling.

Symbol	Quantity	Scaling factor
x, y, z	Cartesian coordinates	h
	z positive upwards from bottom	
$\mathbf{e}_x, \mathbf{e}_y, \mathbf{e}_z$	unit vectors	
a, b, h	length, width, height	h
k	wavenumber in x	π/a
l	wavenumber in y	π/b
t	time	h^2/κ
$\mathbf{v} = (u, v, w)$	velocity	κ/h
$\dot{\varepsilon}_{ij}$	strain rate	κ/h^2
τ_{ij}	deviatoric stress	$\eta_0\kappa/h^2$
ϕ	poloidal potential	κh
ψ	toroidal potential	κ
T	temperature	ΔT
ΔT	temperature contrast	
Q	volumetric rate of heating	$\kappa\rho c_p \Delta T/h^2$
η	viscosity	η_0
η_0	reference viscosity	
B, Θ	viscosity parameters (equations 19, 20)	
r	viscosity ratio (equations 19, 20)	
s	viscosity ratio (equation 22)	
κ	thermal diffusivity	
c_p	specific heat	
α	thermal expansion coefficient	
ρ	density	
g	gravity acceleration	
Ra	Rayleigh number	$Ra = \alpha g \rho \Delta T h^3/(\kappa\eta_0)$

Definition of operators:

$\nabla^2 = \partial_{xx} + \partial_{yy} + \partial_{zz}$ Laplacian
$\Delta_2 = \partial_{xx} + \partial_{yy}$ horizontal Laplacian
$F = \partial_{yy} - \partial_{xx}$
$G = \partial_{zz} - \Delta_2$

$$\dot{\varepsilon}_{xz} = \partial_x G\phi + \partial_{yz}\psi, \tag{8d}$$

$$\dot{\varepsilon}_{xy} = 2\,\partial_{xyz}\phi + F\psi, \tag{8e}$$

$$\dot{\varepsilon}_{yz} = \partial_y G\phi - \partial_{xz}\psi, \tag{8f}$$

and the components of the vorticity $\boldsymbol{\omega} = \nabla \times \mathbf{u}$ are

$$\omega_x = -\partial_y \nabla^2 \phi + \partial_{xz}\psi, \tag{9a}$$

$$\omega_y = \partial_x \nabla^2 \phi + \partial_{yz}\psi, \tag{9b}$$

$$\omega_z = -\Delta_2\psi. \tag{9c}$$

For the purpose of numerical treatment the viscosity is split at each horizontal level into a mean part and a fluctuating part:

$$\eta(x, y, z) = \bar{\eta}(z) + \tilde{\eta}(x, y, z). \tag{10}$$

The equation for the toroidal potential is obtained by taking the z-component of the curl applied to equation (2). The result is then manipulated in such a way that the terms involving the mean viscosity are kept on the left-hand side, where the strain rate is resolved into the potentials by using equation (8), and where the poloidal potential drops out. The terms involving the fluctuating viscosity are written on the right-hand side (RHS) without resolving the strain rate:

$$[\bar{\eta}\,\partial_{xx} + \bar{\eta}\,\partial_{yy} + \partial z(\bar{\eta}\,\partial_z)]\Delta_2\psi = \partial_{xy}[\tilde{\eta}(\dot{\varepsilon}_{yy} - \dot{\varepsilon}_{xx})]$$
$$-F(\tilde{\eta}\,\dot{\varepsilon}_{xy}) + \partial_{xz}(\tilde{\eta}\,\dot{\varepsilon}_{yz}) - \partial_{yz}(\tilde{\eta}\,\dot{\varepsilon}_{xz}). \tag{11}$$

Taking the z-component of the curl of the curl of equation (2) and manipulating it accordingly provides the equation for the poloidal potential:

$$G(\bar{\eta}\,G)\Delta_2\phi + 4\,\partial_z\Delta_2(\bar{\eta}\,\partial_z)\Delta_2\phi = -\partial_x G(\tilde{\eta}\,\dot{\varepsilon}_{xz})$$
$$-\partial_y G(\tilde{\eta}\,\dot{\varepsilon}_{yz}) + 3/2\,\partial_z\Delta_2(\tilde{\eta}\,\dot{\varepsilon}_{zz}) - 2\,\partial_{xyz}(\tilde{\eta}\,\dot{\varepsilon}_{xy})$$
$$-1/2\,\partial_z F[\tilde{\eta}(\dot{\varepsilon}_{yy} - \dot{\varepsilon}_{xx})] + Ra\,\Delta_2 T. \tag{12}$$

When the viscosity is a function of depth only, there is no source term in (11) and the toroidal potential is zero for homogeneous boundary conditions, while the only source for the poloidal potential is the buoyancy term involving the Rayleigh number in (12). In the general case of laterally varying viscosity the terms on the RHS of (11) and (12) describe the coupling of poloidal and toroidal motion. The boundary conditions at the top and bottom boundary, $w = 0$ and either $u = v = 0$ (rigid) or $\tau_{xz} = \tau_{yz} = 0$ (stress-free), translate into

$$\phi = \partial_z \phi = \psi = 0 \quad \text{(rigid)}, \tag{13a}$$

or

$$\phi = \partial_{zz}\phi = \partial_z\psi = 0 \quad \text{(free)}, \tag{13b}$$

and for the temperature the boundary conditions are

$$T(x, y, 0) = 1 \quad \text{and} \quad T(x, y, 1) = 0. \tag{13c}$$

Note: although the operator in equation (12) is of sixth order, it contains derivatives in z up to the fourth order only, therefore two conditions on each boundary are sufficient; the fourth-order operator in (11) has only

second-order derivatives in z and one condition on each side is enough.

The set of equations, which are to be solved numerically, consists of equation (5) combined with (7a–c), equation (11) and (12) combined with (6), (8a–f), and 10. It is assumed that the solution exhibits translational symmetry (periodicity) in the Cartesian x- and y-directions, with the translation vectors for a unit cell being $2a\,\mathbf{e}_x$ and $2b\,\mathbf{e}_y$. With the proper choices for a and b this allows us to study, besides 2-D rolls, square cells for $a = b$, hexagons or triangles for $b = a/\sqrt{3}$, or general bimodal flow for any $b \neq a$.

A hybrid spectral and finite difference method is employed. The equispaced finite difference grid is defined for a rectangular box of the size $a \times b \times 1$; the assumed symmetry of the solution is equivalent to taking reflecting side boundaries. The temperature equation (5) is advanced in time by an ADI finite difference scheme. A Douglas–Brian-split (Lapidus & Pinder 1982) is used, which remains stable for time steps considerably larger than the Courant time step. This is useful when only a stationary solution is sought, as we did in most of the case studies. In these cases the time step Δt was typically limited by a criterion of the kind $max\,(|\mathbf{v}|\,\Delta t) = t_s < 1$. The left-hand sides of (11) and (12) are Fourier transformed in the x- and y-direction. The assumed periodicity allows to use only sine terms for ψ and cosine terms for ϕ and T. A set of decoupled ordinary differential equations (ODEs) in z for each spectral mode k, l is obtained:

$$d_z(\overline{\eta}\,d_z\Psi_{kl}) + (k^2 + l^2)\overline{\eta}\Psi_{kl} = 1/(k^2 + l^2)ST_{kl}(\cdots), \quad (14)$$

$$(d_{zz} + k^2 + l^2)[\overline{\eta}(d_{zz} + k^2 + l^2)\Phi_{kl}]$$
$$-4(k^2 + l^2)d_z(\overline{\eta}\,d_z\Phi_{kl}) = Ra\,T_{kl} + 1/(k^2 + l^2)ST_{kl}(\cdots), \quad (15)$$

where $ST_{kl}(\cdots)$ stands for the kl-mode of the spectral transform of the terms involving the strain rate on the RHS of (11) and (12), respectively. The ODEs are solved by a finite difference method, leading to sets of tridiagonal and pentadiagonal matrices. When the viscosity is constant or only a function of depth, equation (14) can be dropped and the solution to (15) is immediately obtained without iteration, because the last term on the RHS is zero and the spectral modes are all decoupled. In case of variable viscosity, first the strain rate is calculated in each grid point by finite differencing the solution for ϕ and ψ obtained in the previous iteration step. In order to avoid the need for taking third-order differences, $\partial_x\phi$ and $\partial_y\phi$ are calculated in spectral space, inversely Fourier transformed, and then second-order differencing is done on the physical grid. The strain rate is multiplied with $\overline{\eta}$ and second-order finite differencing of the result is performed in the physical space; then the result is transformed to spectral space, where the final differentiation with respect to x and y is done by multiplying with k and l, respectively, to obtain the RHS of equation (15).

After each update of the temperature and viscosity, a subiteration is performed on equations (14) and (15) (for strain-rate-dependent viscosity, the viscosity is continuously updated during this subiteration). When we consider only stationary solutions, the subiteration is restricted to five

steps rather than driving it to convergence for each instant of time during the transient evolution. The definition of the mean viscosity $\overline{\eta}(z)$ is important for the iterative solution of the variable viscosity problem. In principle, the splitting in equation (10) can be done for arbitrarily defined $\overline{\eta}$. Initially we employed the arithmetic mean, which was used for most results that are presented here. In this case relaxation is needed during the subiteration to ensure stability. Empirically it was found that the higher harmonics need a stronger relaxation and that a limited overrelaxation with the solution before the last one enhances convergence. When the superscript denotes the iterative step, the solution was relaxed by

$$^i\Phi_{kl} = (1 - q_{kl} + q_u)^i\Phi_{kl} + q_{kl}{}^{i-1}\Phi_{kl} - q_u{}^{i-2}\Phi_{kl}, \quad (16a)$$

$$q_{kl} = q_0[1 - (k + l + kl)^{-1}], \qquad q_u = q_0/2, \quad (16b)$$

with an expression equivalent to (16a) for Ψ. For q_0 values of 0.5–0.9 were chosen. For 3-D flow with rigid boundaries the iteration for solving the mode-coupling through lateral viscosity differences remains stable for a total top-to-bottom *viscosity contrast up to 100 for the given choice of $\overline{\eta}$*. On fixed horizontal levels, the maximum viscosity contrast is 25 in this case. For stress-free boundaries, the limit is reached already for a total variation of 40, which again means a maximum lateral variation of about 25.

While a preliminary version of this paper was under review, we realized that taking the average of the maximum and the minimum viscosity at a given horizontal level for $\overline{\eta}$ makes the iteration stable for perhaps unlimited viscosity contrasts. This choice shifts $\overline{\eta}$ to higher values compared to the arithmetic mean. No underrelaxation is needed [$q_{kl} = 0$ in equation (16a)], and some overrelaxation with the next-to-last solution speeds up the convergence ($q_u \approx 0.5$). We have included one example with a global viscosity contrasts of 1000 or a maximum lateral contrast of 75. On the other hand the accuracy of the solution, especially regarding local velocity values as for example the peak velocity in plumes, is somewhat degraded compared to the case where the arithmetic mean is used for $\overline{\eta}$.

As initial condition for the temperature field we took the conductive solution with a perturbation comprising a few basic modes superimposed:

$$T(x, y, z) = (1 - z) + \sum c_{kl} \cos{(k\pi x/a)} \cos{(l\pi y/b)} \sin{(\pi z)}. \quad (17)$$

For stationary solutions, convergence is assumed, when the rms change in the temperature field from one step to the next has fallen below 10^{-6}. Depending on the Rayleigh number, and the character of the solution, convergence is achieved typically within 50–300 steps, faster for 2-D flow, but slower near stability boundaries.

For constant viscosity the numerical method has been verified by comparison with published results (see next section), and with results obtained by Cserepes (personal communication 1989) with a similar numerical method. For roll-type solutions with variable viscosity, a comparison has been done with the results from well-established and precise 2-D codes, with good agreement being found. In the only published numerical work on 3-D variable viscosity convection by Busse & Frick (1985) no quantitative values are listed, but their contour plot for the vertical velocity at

mid-depth for a square cell flow at a viscosity contrast of 11 is found to be in satisfactory agreement with our result.

In addition to these comparisons an internal consistency check is performed on the code, by comparing the total frictional energy dissipation with the Nusselt number Nu, for which the following relation exists (Parmentier *et al.* 1976):

$$Nu - 1 = (Ra\,ab)^{-1} \int \tau_{ij}\dot{\varepsilon}_{ij}\, dV. \tag{18}$$

The equality is fulfilled to within 5 per cent in all cases, and the misfit drops to less than 1 per cent when higher resolution is employed. Comparisons of results obtained on successively finer grids confirm a second-order convergence of the method.

3 RESULTS

3.1 Constant viscosity

In order to verify the numerical method a comparison has been done with results obtained by Frick *et al.* (1983) with a Galerkin method for bimodal convection between rigid boundaries. For a half-wavelength of the primary roll of $a = 1.0079$ the existence of bimodal solutions is investigated for various wavenumbers of the secondary cross-roll at Rayleigh numbers of 26 000 and 30 000. A grid of $16 \times 16 \times 32$ points has been used for the calculations. Our results are in satisfactory agreement with the parameter range that Frick *et al.* determined for the existence of bimodal solutions (Fig. 1), the only difference being that in our case the range seems to be shifted very slightly towards higher wavenumber of the secondary roll. A quantitative comparison of the Nusselt number for a bimodal case with the data by Frick *et al.* is found in Table 2. Trials with different grids suggest that a high resolution in the z-direction is more important than in the horizontal direction. Jarvis & Mitrovica (1989) found the same rule for determining the Nusselt number from finite difference solutions of 2-D convection.
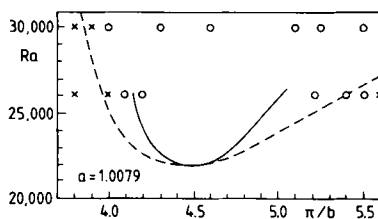

Figure 1. Existence of bimodal convection with constant viscosity. O: bimodal solution, ×: no bimodal solution. The broken line is the limit of existence according to Frick *et al.* (1983), the full line their limit of stability.

3.2 Temperature-dependent viscosity

We take an Arrhenius-type law for the temperature dependence of viscosity. Equation (6) takes the form

$$\eta = \exp\left[B/(\Theta + T) - B/(\Theta + 0.5)\right]. \tag{19}$$

The reference viscosity η_0 (for which the non-dimensional value is $\eta = 1$) is the value at the mean of the top and bottom temperatures and the Rayleigh number is defined with this viscosity value, as it has become a standard convention for bottom heated convection with variable viscosity (Booker 1976; Richter, Nataf & Daly 1983). In order to reduce the number of free parameters in (19), the following expressions are adopted:

$$B = 225/\ln(r) - 0.25 \ln(r), \qquad \Theta = 15/\ln(r) - 0.5, \tag{20}$$

where r is the ratio of the viscosities at the minimum and maximum temperatures. This leads for a given r to a viscosity dependence very similar to that which applies for fluids with strongly temperature-dependent viscosity, such as corn syrup or glycerol, which have been used in laboratory experiments on convection.

3.2.1 Stability of square cell convection

A square pattern of convection, where a columnar upwelling is surrounded by descending sheet-like flow, becomes stable when the viscosity is temperature dependent (Busse & Frick 1985). White (1988) has performed a very detailed and systematic laboratory investigation of the stability of rolls, squares, and other planforms of convection, using corn syrup as a working fluid. Partially in order to test our code, we tried to reproduce White's stability diagram, by calculating solutions in a cube ($a = b = 1$) with rigid top and bottom boundaries (abbreviated RR). Cases with identical parameters were started from two different initial conditions, a nearly roll-like initial perturbation as $c_{10} = 0.1$, $c_{01} = 0.001$ in equation (17), and a nearly square condition like $c_{10} = 0.1$, $c_{01} = 0.099$. As a rule, during the iteration there was first convergence towards the initialized pattern, but, if this pattern was unstable, a transient stage of divergence is found until the system finally settles into the preferred stable stationary pattern. The complete evolution into the final pattern was only followed in a few cases when the intialized planform turned out to be unstable, and often only the growth of the perturbation was recorded. Of course, this is only a partial test of stability, as only such perturbations are possible which fit the assumed periodicity. In the case of a cube basically squares or rolls are possible, when excluding a type of bimodal flow where the wavelength is the same in both directions but the amplitudes differ.

We find that squares become stable at viscosity contrasts

Table 2. Convergence test.

Ra = 30,000 const η RR a=1.0079 b=0.6283 bimodal flow

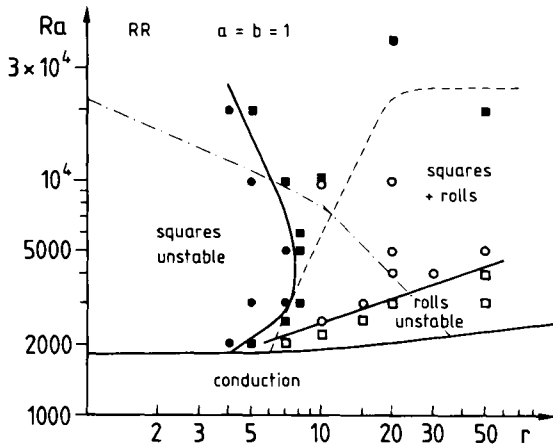| Frick et al.				this work			
nodes	Nu	grid	Nu	v_rms	grid	Nu	v_rms
8	3.652	8x8x8	4.39	47.5	8x8x16	not bimodal	
10	3.587	16x16x16	3.786	42.67	16x16x32	3.562	41.39
12	3.563	32x32x32	3.597	41.27	32x32x64	3.544	40.97

Figure 2. Stability of squares with rigid boundaries and variable viscosity. ■: squares stable in respect to decay into rolls, O: roll stable with respect to transition into square, □: roll transforms to square, ●: square changes into roll. The dashed line is the stability limit for squares according to White (1988), the dot–dashed his limit for rolls.

between 5 and 8, depending on the Rayleigh number (Fig. 2). For Rayleigh numbers up to 6000 this is in fair agreement with White's (1988) experimental results. At higher Rayleigh number and $r \leq 10$ White found that squares break down into a bimodal flow pattern. In our computational setting bimodal flow would only be possible

with a half-wavelength of 0.5 for the secondary roll, but such a pattern did not occur even when an appropriate perturbation was imposed on the temperature. White (1988) found a half-wavelength of about 0.8 for the secondary roll. As such a bimodal flow is not possible in our case, the stability limit (which is actually the limit for the breakdown of squares into rolls) diverges from White's boundary. Our limit for the breakdown of rolls into squares, however, is completely different compared to White's result (Fig. 2). At Rayleigh numbers above 7000 and $r > 10$ White found that rolls first become bimodal before they subsequently transform into squares. This may explain why we find rolls to be stable in this range. The range $Ra_{crit} < Ra < 3000$ and $5 < r < 30$, where we find break-down of rolls into squares, whereas White marks it as region of stable rolls, was actually not covered by a laboratory experiment. Still, there remains a discrepancy in the range $Ra = 3000$–6000 and $r > 20$, where the laboratory data indicate a direct transformation from rolls to squares, whereas we find rolls to be stable. It is not clear at the moment how to explain this disagreement. However, we note that our diagram is in agreement with the principal geometry of stability regions as found by Busse & Frick (1985) for temperature-dependent viscosity. Their boundaries are shifted towards lower viscosity ratios compared to ours, which is undoubtedly due to the difference in the viscosity law, because they used a linear dependence of viscosity on temperature.

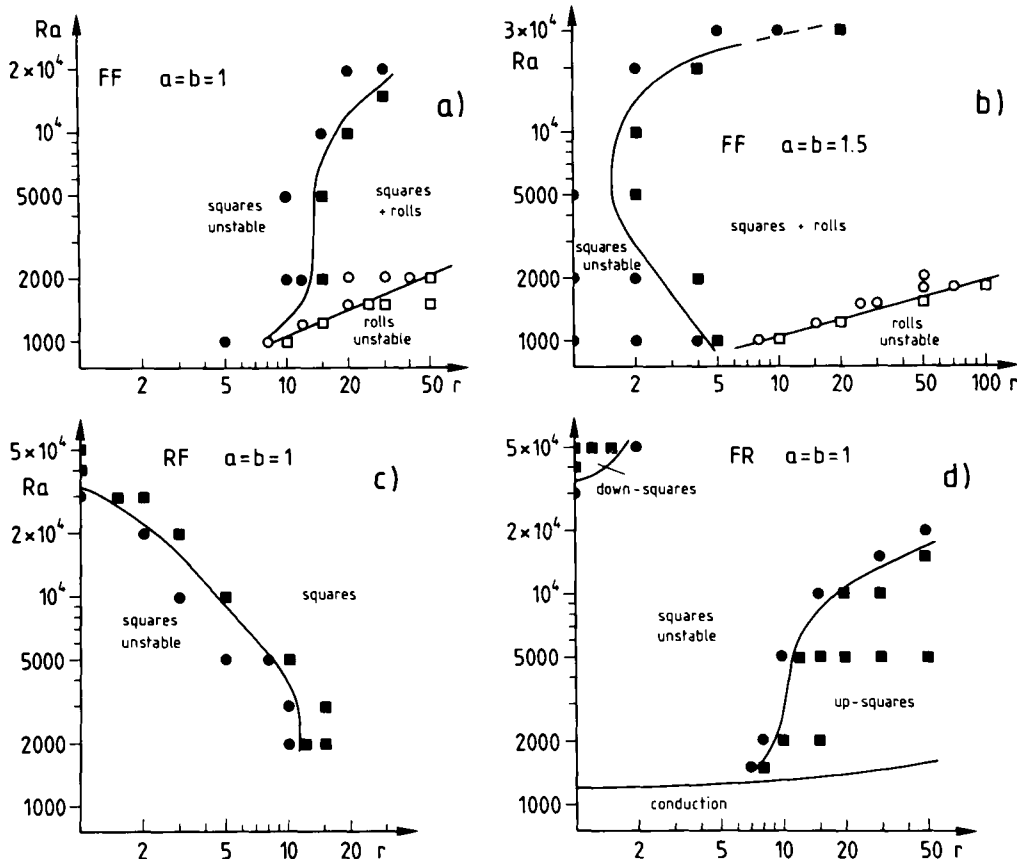The stability diagrams for stress-free upper and lower

Figure 3. Stability diagram for squares with free and mixed boundary conditions. See Fig. 2 for symbols. (a) Free boundaries, cubic cell. (b) Free boundaries, size $a = b = 1.5$. (c) Upper boundary rigid, lower boundary free, cubic cell. (d) Upper boundary free, lower boundary rigid, cubic cell.

boundaries (abbreviated FF) are shown in Fig. 3. Besides the case with $a = b = 1$, also that for $a = b = 1.5$ has been studied, which is close to the critical wavelength at the onset of convection for variable viscosity (Stengel, Oliver & Booker 1982). In the latter case squares become stable already for a viscosity contrast of two at Rayleigh numbers in the range of 5000–10 000. Contrary to the case of rigid boundaries, however, we find that above $Ra = 10\,000$ increasingly higher viscosity ratios are needed to prevent the breakdown of squares into rolls. The boundary for the instability of rolls is similar as in the rigid case.

When the upper boundary is rigid and the lower boundary is free (RF, Fig. 3c), a square pattern is stable even for constant viscosity, when the Rayleigh number exceeds about 30 000 (for $a = b = 1$), in agreement with the results of Cserepes *et al.* (1988). At low Rayleigh number a viscosity contrast of up to 12 is needed to stabilize the square pattern. For the upper boundary rigid and the lower one free (FR, Fig. 3d) the diagram looks generally similar to the FF case, except for a slight shift of the stability field of squares towards higher viscosity ratios. Besides squares with a rising columnar plume ('up-squares') found at high viscosity contrasts, squares with a sinking columnar jet ('down-squares') are stable at $Ra > 35\,000$ and very weak or

vanishing viscosity variation as a consequence of the rigid boundary condition on the side of the hot boundary layer. The influence of temperature-dependent viscosity, which favours up-squares, acts to destabilize the down-squares.

To summarize the results: squares are a stable flow pattern with respect to the decay into rolls (but not necessarily against other 3-D pattern, like bimodal, hexagonal, or spoke pattern) for modest viscosity contrasts of the order 10 or higher, especially for a rigid upper boundary condition. Higher Rayleigh numbers, in excess of 10^4, have an adverse influence on the stability of squares when the upper boundary is stress-free.

3.2.2 Properties of square cell convection

Solutions for square cell convection with rigid top and bottom boundaries have been calculated in the range between 10^4 and 10^5 for the Rayleigh number and viscosity ratios from 5 to 100. For most of the calculations a grid of $16 \times 16 \times 32$ has been employed. Convergence tests in a few cases suggest that this gives adequate resolution for Rayleigh numbers of the order of 3×10^4, whereas at $Ra = 100\,000$ a grid of $32 \times 32 \times 64$ is necessary to keep the errors at a tolerable level (Table 3). Although with rigid

Table 3. Properties of squares with rigid boundaries.

r	Nu	$<T>$	v_{rms}	v_t	[%]	w_u	w_d	R_w
			Ra=10,000					
10	2.60	.536	21.4	1.4	1.9	3.46	1.63	0.40
30	2.51	.557	22.4	1.6	2.4	3.76	1.34	0.55
50	2.47	.566	23.0	1.6	2.5	3.87	1.21	0.63
100	2.41	.578	24.0	1.5	2.4	4.01	1.06	0.73
			Ra=20,000					
5	3.20	.518	33.8	0.9		4.11	2.07	0.34
10	3.14	.536	34.6	1.1	1.9	4.42	1.88	0.40
20	3.07	.553	35.7	1.3	2.3	4.67	1.67	0.47
30	3.03	.563	36.5	1.4	2.5	4.81	1.56	0.53
50	2.97	.574	37.7	1.5	2.7	5.00	1.46	0.56
75	2.93	.582	38.7	1.5	2.8	5.11	1.37	0.62
100	2.90	.588	39.5	1.5	2.9	5.19	1.29	0.65
			Ra = 30,000					
5*	3.49	.514	42.5	0.7	1.5	4.63	2.21	0.33
10	3.42	.530	42.5	0.9	1.7	4.85	2.03	0.38
10*	3.40	.529	42.0	1.0	1.7	4.83	2.02	0.38
30	3.35	.563	47.5	1.2	2.4	5.51	1.73	0.50
100	3.20	.591	51.6	1.5	2.8	5.91	1.45	0.61
100*	3.18	.589	51.0	1.5	2.9	6.04	1.45	0.60
100**	3.17	.588	50.7	1.5	2.8	6.09	1.44	0.59
1000	2.98	.634	61.0	1.7	3.3	5.32	1.21	0.73
1000*	2.96	.629	60.8	1.7	3.3	5.91	1.16	0.75
1000**	2.95	.628	60.8	1.7	3.3	6.21	1.14	0.75
			Ra = 30,000	with internal heating	Q=3			
30	4.49	.747	50.9	1.8	3.7	3.54	2.75	0.63
			Ra = 50,000					
5	4.10	.503	64.0	0.5	1.3	5.74	2.44	0.33
10	3.91	.527	61.2	0.8	1.5	5.91	2.19	0.38
30	3.78	.562	65.1	1.1	2.3	6.34	1.92	0.47
50	3.70	.576	67.5	1.3	2.7	6.45	1.81	0.52
100	3.61	.598	71.2	1.5	3.3	6.42	1.70	0.56
			Ra = 100,000					
10	4.64	.533	93.1	0.8	1.7	6.23	2.41	0.39
10*	4.54	.519	90.3	0.6	1.4	6.93	2.37	0.38
10**	4.52	.517	89.6	0.6	1.4	7.05	2.37	0.38
30	4.54	.596	101.3	1.9	3.7	5.42	2.34	0.39
50	4.50	.624	106.2	2.7	4.7	4.96	2.39	0.36
100	4.43	.655	113.5	3.5	6.2	4.60	2.47	0.32
100*	4.31	.637	110.3	2.8	5.2	5.28	2.27	0.36
100**	4.27	.628	108.8	2.6	4.9	5.61	2.19	0.38

($<T>$ - mean temperature; v_t - ratio of toroidal to total velocity (rms-values), first number is global ratio, second for horizontal level with max. value; w_u - max. rising, w_d - max. sinking velocity at z=0.5 relative to global rms-velocity; R_w - ratio of min. to max. velocity in descending sheets at z=0.5; the grid is 16x16x32, except where indicated by (*) [24x24x48] or by (**) [32x32x64])
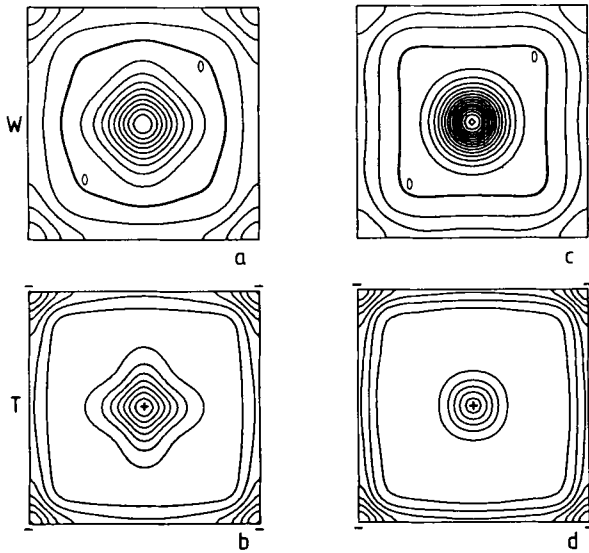

Figure 4. Isotherms and contours of vertical velocity (w) for square cell convection in a horizontal plane at $z = 0.5$. Rigid boundaries, $a = b = 1$, $Ra = 30\,000$. The actual calculation was performed on one quarter of the figure shown, which was then completed according to the assumed symmetry. (a) $r = 5$, $w = -80\cdots$ $(+20)\cdots + 180$, (b) $r = 5$, $T = 0.20\cdots(+0.05)\cdots 0.85$, (c) $r = 100$, $w = -60\cdots(+20)\cdots + 300$, (d) $r = 100$, $T = 0.35\cdots$ $(+0.05)\cdots 0.90$.

boundaries squares are actually unstable to spoke-flow for $Ra > 25\,000$ (White 1988), it could give some insight to compare the change in properties for a well-defined flow pattern over a sufficiently large range of Rayleigh numbers.

Figure 4 shows horizontal cross-sections through square cells at mid-depth for viscosity contrasts of $r = 5$ and 100 at a Rayleigh number of 30 000. In both cases, the upwelling flow takes the form of a plume and the descending flow is sheet-like. At the lower viscosity ratio, the descending flow has a stronger tendency to concentrate in falling jets at the crossing points of the sheets, and the plume shows significant deviation from circularity. With increasing viscosity contrast, the velocity in the sheets becomes more uniform, and also the plume approaches more closely a circular geometry. In general the descending sheets are more uniform at shallow depth, whereas they tend to concentrate into jets near the bottom (see also Bercovici et al. 1989a).

Some properties of interest are listed in Table 3 for RR conditions and in Table 4 for stress-free or mixed boundary conditions. The principal effect of variable viscosity seems to be independent of the type of boundary condition. The Nusselt number is weakly decreasing with the viscosity ratio and the mean temperature in the cell rises, in accord with the experimental results by Booker (1976) and Richter et al. (1983). With increasing r, generally the maximum descending velocity decreases, whereas the ratio of minimum to maximum velocity R_w in the descending sheets rises to values closer to unity. At mid-depth the maximum velocity in the ascending plume is about 4–6 times the rms velocity of the flow. It is found to increase only weakly with the global viscosity contrast in the range $5 < r < 1000$ (Tables 3 and 4). The reason is that the difference between the viscosity in the centre of the plume and the mean

Table 4. Squares with stress-free and mixed boundaries.

r	Nu	$\langle T \rangle$	v_{rms}	$v_l[\%]$		w_u	w_d	R_w
			FF $a=b=1$	Ra = 20,000				
30	5.58	.560	66.6	1.4	3.2	4.62	1.43	0.24
			FF $a=b=1.5$	Ra = 20,000				
3	5.75	.448	75.5	0.4	0.7	4.33	1.74	0.40
10	5.59	.469	73.5	0.8	1.5	5.17	1.35	0.45
20	5.41	.487	72.0	0.9	1.8	5.62	1.17	0.50
30	5.28	.501	71.2	0.9	1.8	5.83	1.07	0.53
40	5.18	.513	70.6	0.9	1.8	5.95	1.00	0.55
			RF $a=b=1$	Ra = 20,000				
3	4.10	.598	48.8	0.5	1.0	3.32	2.32	0.28
20	3.69	.635	53.2	1.2	2.6	4.00	1.71	0.47
50	3.51	.651	56.5	1.4	3.0	4.23	1.49	0.57
			FR $a=b=1$	Ra = 15,000				
50	3.82	.497	37.1	1.7	3.1	4.94	1.21	0.33

(see Table 3 for explanations)

viscosity at the same z-level rises only from 2 to 3 between $r = 10$ and 100 (at $Ra = 30\,000$). The viscosity difference is so weak because (i) with the assumed viscosity law a given ΔT will produce less viscosity variation at high temperature than at low temperature, and (ii) because the temperature in the core of the convection cell rises with increasing r, which reduces the temperature difference across the lower boundary layer and consequently also between plume and ambient fluid. The rising columns in the centre of the square cells are therefore still different from the narrow conduit-like structures envisaged for plumes in the mantle.

For Rayleigh-numbers exceeding 5×10^4 and high viscosity ratio, the solution changes its character in the RR case (other boundary conditions were not studied at such high Rayleigh numbers). The ascending plume is no longer circular, but becomes clover-shaped (Fig. 5). In the descending sheets additional knots of concentrated downwelling occur. The maximum ascending velocity now rather decreases with increasing r (Table 3). The solution has some
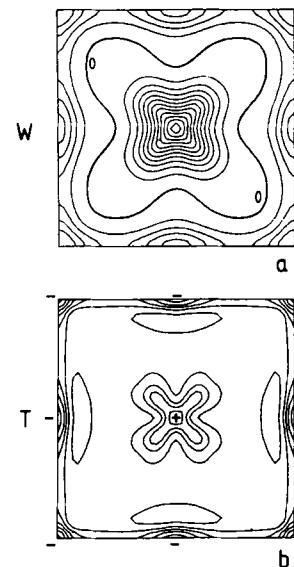

Figure 5. Isotherms and contours of vertical velocity for square cell convection in a horizontal plane at $z = 0.5$. $Ra = 100\,000$, $r = 100$, RR, $a = b = 1$. (a) $w = -200\cdots(+50)\cdots 550$, (b) $T = 0.40\cdots(+0.05)\cdots + 0.85$.

attributes of the spoke-type flow (see below), but which are forced here to fit the square periodicity. Therefore we do not consider this pattern as representative for square-cell convection.

A single square case with a finite rate of internal heating $Q = 3$ has been calculated. The bottom temperature was fixed as usual, and about 2/3 of the total heat was supplied by the internal souces ($Ra = 30\,000$; $r = 30$; RR, $a = b = 1$). A stable square cell was found. The velocity in the rising plume is less than in the purely bottom-heated case, as expected, but there is no higher tendency for the descending sheet to concentrate into jets, i.e. no decrease of R_w compared to the purely bottom-heated case (Table 3). With stress-free boundaries no stationary solution could be obtained. This single result suggests that partial heating from within has no adverse influence on the principal configuration of rising plumes and sinking sheets, as it was also found for constant viscosity convection in a spherical shell (Bercovici *et al.* 1989b).

3.2.3 Comparison of various flow patterns

Besides squares, several other flow patterns observed by White (1988) were reproduced. In a cell of dimensions $b = a/\sqrt{3}$ a hexagonal pattern can be obtained for an initial condition with $c_{11} = A \neq 0$ in equation (17) (setting $c_{20} = A/2$ will enhance convergence), whereas a triangle can be obtained with $c_{11} = -A$, $c_{20} = -A/2$, $c_{02} = A/2$ and $c_{31} = -A/2$. One model cell contains the quarter parts of two different hexagons, or two half triangles, respectively. Triangles seem to be less stable (White 1988); for $a = 2.0$ or smaller no triangular solution could be obtained, and rather a hexagon was finally formed when starting from the 'triangular' initial state. Therefore triangles and hexagons where calculated for $a = 2.4$ at $Ra = 25\,000$ and $r = 50$ (Fig. 6) and compared with the square ($a = b = 1.2$) and roll
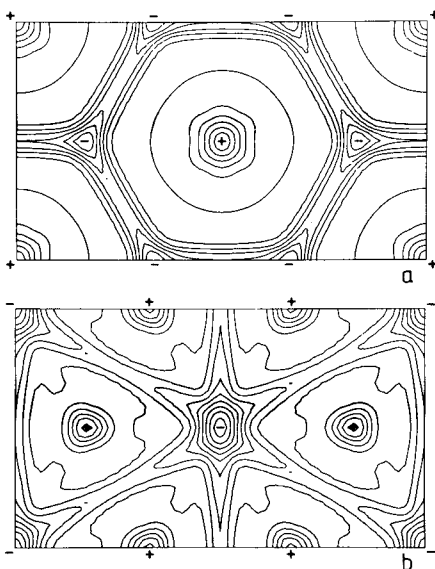
Table 5. Comparison of various flow patterns.

	Nu	\<T\>	v_{rms}	$v_\parallel$[%]		w_u	w_d	R_w
		Ra =25,000	RR	r = 50				
roll	2.90	.611	39.6	0.0	0.0	2.20	1.63	1.0
square	3.03	.580	42.7	1.8	3.2	5.05	1.50	0.63
hexagon	3.01	.577	42.7	0.9	1.2	5.55	1.40	0.72
triangle	3.11	.574	42.6	2.0	4.3	4.95	1.50	0.50
		Ra = 30,000	RR	r=20	a=1.0	b=0.75		
bimodal	3.41	.593	45.3	2.7	5.2	3.90	2.30	-
		Ra = 50,000	RR	r=30	a=4.0	b=4.0		
spoke	3.88	.598	64.3	3.3	6.3	≈4.1	≈2.0	-

(see Table 3 for explanations)

($a = 1.2$) solution. The three 3-D patterns share the principal configuration of a rising jet and sinking sheet-like flow. Their Nusselt numbers, mean velocities and temperatures turn out to very similar, whereas for the roll they are more different (Table 5). Comparing the degree of variation of the descending velocity, i.e. the values of R_w, the hexagon has the most pronounced sheet-like character and at the same time the highest velocity in the ascending plume.

A bimodal solution has been calculated for $a = 1$, $b = 0.75$ at $Ra = 30\,000$ and $r = 20$. It exhibits the typical cross-roll character known from the bimodal pattern at constant viscosity (Fig. 7). The ratio of maximum ascending to maximum descending velocity (at $z = 0.5$) is 1.7, somewhat higher than for a roll of similar viscosity variation, where it is 1.35, but much less than for squares, hexagons, or triangles, where it is in the range of 3–4.

White (1988) found that at $Ra > 25\,000$ the only stable form was a spoke pattern when there was significant viscosity variation. For constant viscosity convection spokes occur only at Rayleigh numbers of 10^5 or more. We did one experiment in a rather large cell with $a = b = 4$ for $Ra = 50\,000$ and $r = 30$, starting with red noise as initial perturbation of the temperature field, and employing a grid of $64 \times 64 \times 32$. After about 50 pseudo-time steps (Δt was 16 times the Courant step) a fairly stable geometric pattern was established, but it did not converge to steady state, which is not surprising, as the spoke pattern is known to be time dependent. Our of fear that the large pseudo-time step would introduce some unphysical features into an unconverged unsteady solution, we continued the iteration for about one overturn time with Δt limited by the Courant criterion. Only some minor rearrangement of the flow pattern was observed during this time interval. At 3/4 of the

Figure 6. Isotherms in horizontal plane $z = 0.5$. $Ra = 25\,000$, $r = 50$, RR, $a = 2.4$, $b = 2.4/\sqrt{3}$. (a) Hexagonal cell, $T = 0.35\cdots(+0.05)\cdots0.90$, (b) triangular cell, $T = 0.25\cdots(+0.05)\cdots0.90$.
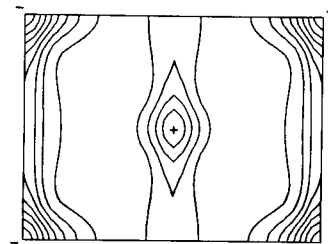

Figure 7. Isotherms in horizontal plane $z = 0.5$ for bimodal flow pattern, $Ra = 30\,000$, $r = 20$, RR, $a = 1$, $b = 0.75$; $T = 0.35\cdots(+0.05)\cdots0.90$.
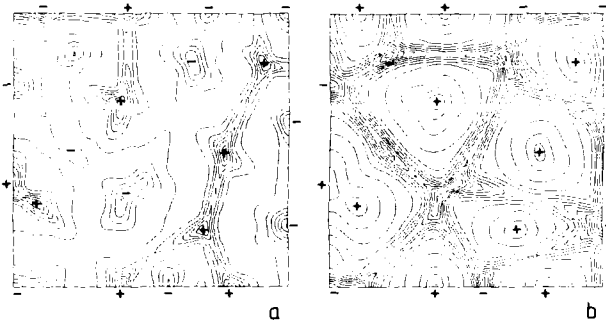
Figure 8. Isotherms in horizontal planes for spoke-pattern flow. $Ra = 50\,000$, $r = 30$, RR, $a = b = 4$. (a) $z = 0.25$, (b) $z = 0.75$.

Figure 9. Total rms velocity (full line), toroidal rms velocity (broken), and maximum-to-minimum lateral viscosity variation ρ (dotted) as a function of depth for square cell flow. Note the tenfold enhancement of scale for the toroidal velocity. (a) $Ra = 30\,000$, $r = 100$, RR, $a = b = 1$. (b) $Ra = 20\,000$, $r = 30$, FF, $a = b = 1.5$.

layer height (Fig. 8b) an irregular polygonal network of descending sheets is found, while the ascending flow is plume-like in the centre of the polygons. At 1/4 height (Fig. 8a), the cold regions have contracted into falling jets with only weak traces of the connecting sheets remaining, whereas the warm rising regions are now partly connected (viewed in 3-D they form a system of ridges, and the peaks in this 'mountain chain' are the base of rising jets). For constant viscosity such a pattern has recently been described by Travis, Weinstein & Olson (1990) and by Houseman (1990). While for constant viscosity there must in principal be (anti)symmetry between warm and cold features, here the rising flow exhibits a higher tendency towards jet-like character and the descending flow towards sheet-like flow. At mid-depth the ratio of maximum rising to maximum sinking velocity is about 2.1, which is intermediate between the ratios for rolls or bimodal flow on one side and for squares or hexagons on the other side. It is expected that for stronger viscosity variation the asymmetry between rising and sinking flow will become more pronounced.

3.2.4 Excitation of toroidal motion

In Tables 3–5 the relative fraction of toroidal motion is indicated, both globally and for the z-level with the maximum toroidal velocity. The toroidal contribution is of the order of a few per cent only, and does not strongly depend on the viscosity ratio for $r > 5$. For example, for squares at $Ra = 30\,000$ the maximum lateral viscosity contrast at a given z-level increases by a factor of 14 between $r = 10$ and 1000, while the toroidal velocity increases by a factor of less than 2. For a given value of r, the toroidal contribution is found to decrease slightly with increasing Rayleigh number, when excluding the case of $Ra = 100\,000$, for which a change in the character of the solution was found. For a Rayleigh number near critical and weak viscosity perturbation, Bolton & Ribe (1989) determined that the toroidal-to-poloidal ratio should increase with the square of the amplitude of the flow and linearly with r. Obviously, saturation of the toroidal motion is nearly reached at fairly moderate viscosity variation and Rayleigh number. The maxima in the depth distribution of toroidal velocity are found in the thermal boundary layers, and usually (but not always) the absolute maximum is found in the upper boundary layer (Fig. 9). When the boundary condition is rigid, the maximum toroidal motion occurs at the bottom of the upper boundary layer. Among the various
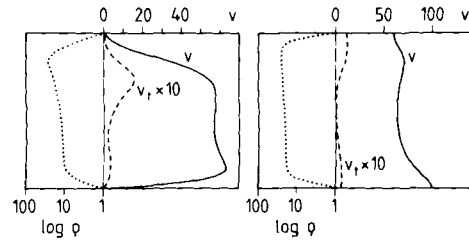
flow geometries, the toroidal-to-poloidal ratio is found to increase in the order roll–hexagon–square–triangle–bimodal–spoke pattern, reaching for the spoke pattern a maximum value of 6.3 per cent at the bottom of the upper boundary layer. Squares are not as efficient in exciting toroidal flow as the bimodal pattern for example, because the lowest toroidal mode with $k = l = 1$, which plays the dominant role in the bimodal case, must be zero for symmetry reasons in the square case.

Obviously not every flow pattern comprises toroidal motion when there are lateral viscosity differences. For example roll-like and axisymmetric flow have zero toroidal motion. Out of the various 3-D pattern that we studied, the hexagon is the closest approximation to axisymmetric flow, and consequently it exhibits the weakest degree of toroidal flow. Squares deviate more strongly from axisymmetry, and triangles even more. Probably lateral viscosity differences are inefficient to generate toroidal motion when they align with the direction of the flow, and viscosity gradients perpendicular to the flow direction are needed. Ricard & Vigny (1989) present an expression where the source term for the vertical vorticity depends on the cross product of pressure gradient and viscosity gradient. Although their formula is an approximation, the implied idea may be correct. For temperature-dependent viscosity, where temperature controls both the driving buoyancy forces and the rheology, strong horizontal viscosity changes will roughly (but not perfectly) align with the horizontal flow direction, and thus only a weak toroidal component can be expected.

Although the toroidal component is very weak by itself, it may play a role in an indirect way. When the toroidal motion is suppressed, i.e. ψ set to zero, but otherwise iterated for ϕ and T in the usual way, the geometry of the rising plume differs appreciably from the complete solution, especially near the bottom (Fig. 10). Suppressing the toroidal motion is artificial, as no longer the physical equations of fluid flow are solved, but it highlights the role of even a weak toroidal velocity component, which feeds back on the poloidal component and the temperature field.

3.4 Non-Newtonian rheology

According to the reasoning in the last section, lateral viscosity variations, which are not directly related to the cause of buoyancy forces, would be more efficient to obtain strong toroidal motion. The simplest kind of rheology which fulfills this condition is a non-Newtonian stress- (or
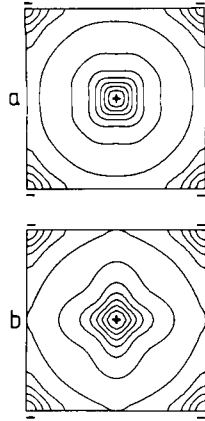
Figure 10. Isotherms at horizontal plane $z = 0.25$ for square cell with $Ra = 30\,000$; $r = 100$, RR, $a = b = 1$. (a) Complete solution, (b) toroidal modes suppressed.

strain-rate-) dependent viscosity. The existence of internally rigid surface plates can lead to a strong toroidal component (Ricard & Vigny 1989), and undoubtedly plate-like behaviour must be due to non-linear creep properties, which facilitate deformation at plate boundaries while keeping the interior of plates nearly rigid.

We have adopted a creep law of the form

$$\eta^*(z, T, \dot{\varepsilon}) = \eta_{\text{newt}}(z, T)(\dot{\varepsilon}/\dot{\varepsilon}_0)^{-(1-1/n)}, \tag{21a}$$

$$\eta = \eta_{\min} + (1/\eta^* + 1/\eta_{\max})^{-1}, \tag{21b}$$

where η_{newt} is the Newtonian viscosity, n the stress exponent in the related stress–strain rate dependence ($\dot{\varepsilon} \propto \tau^n$), $\dot{\varepsilon}$ (without indices) stands for the second invariant of the tensor, and $\dot{\varepsilon}_0$ is a reference value, which is chosen to be approximately the mean strain rate for a particular case. The introduction of $\dot{\varepsilon}_0$ makes the choice of parameter values non-unique, because there is a trade-off between the reference strain rate and the Rayleigh number, but it facilitates the comparison between non-Newtonian cases and their Newtonian counterpart. Because the strain-rate dependence may produce extreme lateral viscosity variations, for example singularities with $\eta = \infty$ where $\dot{\varepsilon} = 0$,

which would be difficult for the numerical scheme to cope with, the viscosity is bounded by minimum and maximum values (equation 21b).

A case study for square cell convection with temperature-dependent non-linear viscosity with $n = 3$ did not reveal a strong enhancement in toroidal motion compared to the purely temperature-dependent case. The square symmetry of the solution may be unfavourable for strong toroidal flow, as discussed in the last section. The same is true for a hexagonal case with free boundaries ($r = 30$, $Ra = 20\,000$). Here the maximum fraction of toroidal flow in the lower boundary layer increased from 1.5 per cent for $n = 1$ to no more than 2.5 per cent for $n = 3$. A case, which was devised as a crude analogue to a lithospheric plate overlying the asthenosphere, turned out to be more interesting. In the Newtonian reference case the viscosity was simply depth dependent:

$$\eta_{\text{newt}}(z) = 1 + (s - 1) \exp\{-[(1 - z)/z_0]^2\}. \tag{22}$$

The size of the cell was chosen to allow for the hexagonal symmetry with $a = 2.4$ and $b = 2.4/\sqrt{3}$ and the boundaries are stress-free. For most of the following cases a grid of $32 \times 16 \times 32$ was employed, which provides sufficient resolution, as one control case with $48 \times 24 \times 48$ suggested. Starting from an initial perturbation of the conductive solution with $c_{11} \neq 0$, a 'down-hexagon' was formed with Newtonian rheology, where the downwelling flow occurred as a jet surrounded by rising sheets; Fig. 11 shows the Newtonian case for $r = 25$, $z_0 = 0.15$, and $Ra = 30\,000$, where the Rayleigh number refers to the viscosity below the high-viscosity lid. With non-Newtonian rheology and starting from the same initial condition, the hexagonal symmetry appeared only for a stress exponent of $n = 2$. As in the non-Newtonian cases with temperature-dependent rheology, the toroidal component is insignificant here (Table 6). For $n \geq 3$, however, a stationary flow pattern emerged which, at the surface, vaguely reminds of two plates moving in anti-parallel direction. In Fig. 12 the case with $n = 6$ is displayed (the highest value of n for which a stable stationary solution was found), with $\dot{\varepsilon}_0 = 80$, $\eta_{\min} = 0.5$, $\eta_{\max} = 50$, and other parameters as above. In the centre,
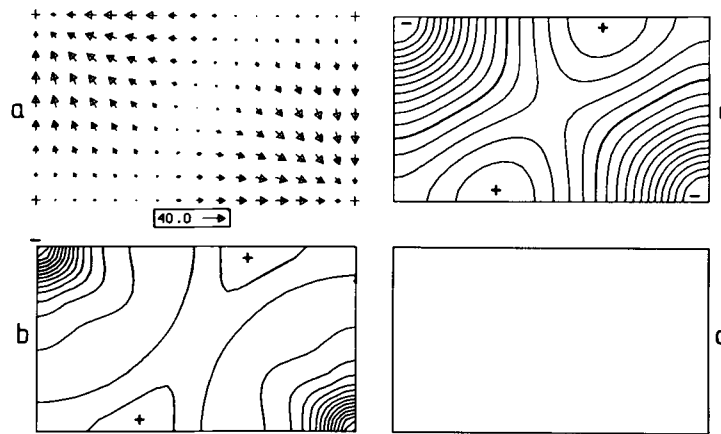

Figure 11. Hexagonal flow with depth-dependent viscosity ($s = 25$) at $Ra = 30\,000$, free boundaries, $a = 2.4$, $b = 2.4/\sqrt{3}$. To complete the hexagon, take mirror images about the lower right or upper left corner. (a) Velocity at surface (sample arrow indicates $v = 40$). (b) Isotherms at mid-depth, $T = 0.15\cdots(+0.05)\cdots 0.90$. (c) Contours of surface divergence, $div = -110\cdots(+10)\cdots + 40$. (d) Vertical vorticity at surface.

Table 6. Convection with non-Newtonian rheology.

n	type	Nu	v_{rms}	$<T>$	$v_t[\%]$		v_{surf}
				Ra=20,000, s=10, η_{max}=50			
1	d-hexagon	3.90	40.4	.656	0.0	0.0	0.58
4	u-hexagon	5.18	57.4	.525	0.7	1.3	0.79
				Ra=30,000, s=25, η_{max}=50			
1	d-hexagon	3.35	39.4	.685	0.0	0.0	0.38
2	d-hexagon	3.94	46.3	.679	0.3	0.4	0.51
3	'plates'	4.18	50.1	.659	5.7	17.7	0.53
4	'plates'	4.39	52.9	.646	6.8	20.3	0.55
6	'plates'	4.60	56.2	.638	7.0	20.1	0.57
				Ra=60,000, s=50, η_{max}=100			
4	'plates'	4.23	68.3	.691	5.3	24.0	0.37
6	'plates'	4.44	72.4	.685	6.0	26.0	0.39

(all cases with ϵ_0= 80, η_{min}=0.5, a=2.4, b=2.4/√3; u=up, d=down, v_{surf} is the rms-velocity at the free surface normalized with the global rms-velocity. For further explanations see Tab. 3)

between the two 'plates', a broad zone of intense horizontal shear is found. The distribution of surface divergence and convergence is more localized than in the Newtonian counterpart, and a significant component of vertical vorticity is found at the surface. The toroidal velocity component is 20 per cent of the total velocity at the surface, and globally it amounts to 7 per cent, which is a threefold enhancement compared to the maximum values found for any of the cases with temperature-dependent viscosity. The toroidal velocity is mainly excited in the surface lid and decays with depth (Fig. 13), as it is the case in models where plate motion is imposed as a velocity boundary condition at the surface (Gable, O'Connell & Travis 1988). A secondary maximum is excited in the lower thermal boundary layer.

In the range n = 3–6, no substantial change in the qualitative pattern, or in quantitative parameter values is found (Table 6). The amount of toroidal energy as function of the exponent n seems to have saturated at n = 6 in the example with s = 25. When the depth-dependent viscosity contrast is increased to s = 50 (equation 24) and the Rayleigh number to 60 000, a slight enhancement of the toroidal-to-poloidal ratio is found at the surface, reaching now 26 per cent for n = 6 (Table 6). A model where the surface lid is formed due to the temperature dependence of
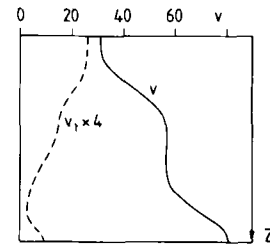
Figure 13. Total rms velocity (full line) and toroidal rms velocity (broken) as function of depth for the non-Newtonian case shown in Fig. 12.

viscosity rather than by an imposed *ad hoc* depth dependence would appear to be more realistic. The reason why the case with temperature-dependent non-Newtonian rheology exhibited the hexagonal flow pattern and not the 'plate' pattern is probably that the viscosity difference between the lid and the underlying cell was too weak. The temperature-dependent ratio of r = 30 means a viscosity difference of the order of only 10 between the maximum at the surface and the value in the core of the cell. In a model with depth-dependent viscosity where the contrast s is only 10, a hexagonal solution was obtained for either Newtonian
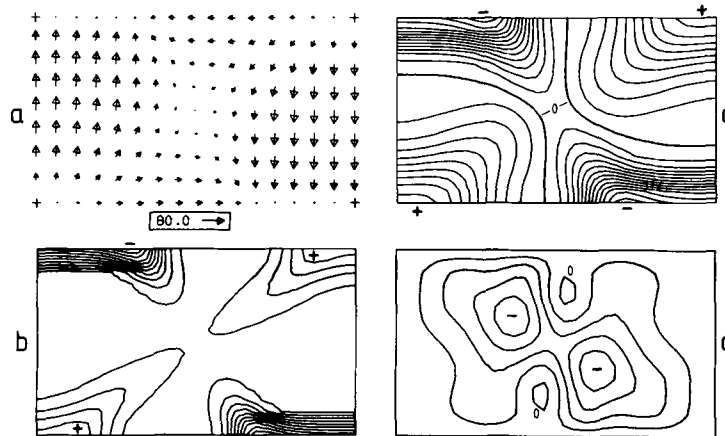
Figure 12. Flow with depth-dependent non-Newtonian rheology, n = 6 and other parameters as in Fig. 11. (a) Velocity at surface, sample arrow indicates v = 80. (b) Isotherms at mid-depth, T = 0.20· · ·(+0.15)· · ·0.90. (c) Surface divergence, div = −260· · ·(+20)· · · + 180. (d) Vertical vorticity at surface, ω_z = −40· · ·(+10)· · ·0.

or non-linear rheology, although there is a change from descending jet-like flow $n = 1$ to an ascending jet with $n = 4$ (Table 6).

4 CONCLUSIONS

Our numerical calculations are done in a parameter range which is quite removed from appropriate parameters for convection in the earth's mantle. The viscosity contrasts are too moderate, and the Rayleigh numbers too small. Nonetheless, for $Ra > 10^4$ the boundary layer structure, which is typical for high Rayleigh number convection, is already present, and the trends observed in our study may give a hint to what could be expected for the mantle convection.

The temperature dependence of viscosity leads at low Rayleigh number to the stabilization of regular 3-D flow patterns, like squares or hexagons, which exhibit plume-like ascending flow, while the descending flow becomes progressively more similar to a sheet as the viscosity contrast rises. This has been known before for rigid boundaries, and is shown here to apply as well for stress-free boundaries. The decay of 2-D rolls into squares was found only for low Rayleigh number and high viscosity differences, in contrast to previous experimental work. An explanation could be that the imposed symmetry in the numerical study does not allow for the transition mechanisms which act in a large plane layer. At Rayleigh numbers >30 000, an irregular and time-dependent spoke pattern had previously been found to be the preferred solution with variable viscosity. Here, we find a network of sinking sheets at shallow depth breaking up into single falling jets at greater depth. In contrast to the regular flow patterns (squares, etc.), also the rising flow forms a system of connected sheets or 'ridges' near the bottom, which at greater height breaks apart into isolated plumes. However, the temperature dependence of viscosity causes an asymmetry, making the jet-like character more prominent for the ascending flow and the sheet-like character more pronounced for the sinking flow. This dichotomy will probably become stronger for increased viscosity differences.

These results strengthen the case that in the earth's mantle plumes should be the preferred mode of upwelling, and sheets the pattern of downwelling. Thus a variety of circumstances, which are all relevant for mantle convection, favour this particular scenario: spherical geometry (Bercovici *et al.* 1989a, b), a low-viscosity layer in the uppermost mantle due to the pressure-dependence of viscosity or due to partial melt (Cserepes & Christensen 1990), and the temperature-dependence of viscosity (Busse & Frick 1985; White 1988; and this work). In the case of upper mantle convection limited by the 670 km discontinuity the sphericity would be much less important than for whole mantle convection, but for the two last-named reasons rising plumes and sinking sheets would still be expected. Considering that the spoke pattern is favoured by both high Rayleigh number and by variable viscosity, it appears possible that mantle plumes are connected by a network of sheets or 'ridges' near the base of the convecting layer. This possible geometry should for example be considered when trying to interpret the laterally heterogeneous seismic velocity structure of the D″ layer at the core-mantle boundary (e.g. Haddon &

Buchbinder 1987). A recent discussion of this particular flow geometry is also given by Houseman (1990).

The ratio of the velocity in the rising plume to the mean velocity increases only slightly with increasing temperature dependence of viscosity in our case studies, because the difference in viscosity between the plume and its exterior never exceeded a factor of 3. Therefore these plumes are still fairly wide columns unlike the envisaged narrow and fast low-viscosity conduits which are considered for mantle plumes (Loper & Stacey 1983; Olson & Christensen 1986), and which exhibit interesting phenomena, like propagation of disturbances as solitary waves. Although in our numerical calculations the temperature dependence of viscosity is still weak compared to that anticipated for the mantle, it will remain a problem to obtain a viscosity contrast of several orders of magnitude between plume and ambient mantle (e.g. Nataf 1990), because the ΔT across the lower boundary layer from which plumes arise is bound to remain fairly small due to the drop in viscosity. The ΔT could be increased and thus plumes could be made relatively hotter, faster, and narrower when the viscosity above the boundary layer was very high, for example because of a strong pressure dependence of viscosity (Christensen 1985) or by the presence of very cold descended slab material (Nataf 1990).

For a variety of 3-D flow patterns the proportion of toroidal motion in the velocity field is found to remain at a level of only a few per cent with temperature-dependent viscosity. For Rayleigh numbers $>10^4$ and viscosity contrasts greater than 10 it does not strongly depend on either viscosity contrast or Rayleigh number. Therefore we expect that the variation of viscosity due to temperature differences is unlikely to excite a significant toroidal flow in the mantle, and certainly it will be insufficient to create the strong toroidal component found at the earth's surface. On the other hand, we have shown that the introduction of a non-Newtonian stress dependence in the creep law can lead to appreciable toroidal velocity in some cases. Although in our models the toroidal component did not reach quite the same size as the poloidal component at the free surface, the observed trend suggests that an equipartioning could be achieved for a higher Rayleigh number and/or stronger depth or temperature dependence of viscosity than we employed, in conjunction with a strong non-linearity of the creep law. In our models with a high-viscosity lid, the toroidal flow is mainly excited in the lid. At the same time the zones of surface divergence and convergence become narrower than they are for Newtonian rheology, which was already found in 2-D models with non-linear rheology (Christensen 1984a). The vertical vorticity, on the other hand, was less localized in our models.

These results support the assumption (Forte & Peltier 1987; Gable *et al.* 1988) that the toroidal motion at the earth's surface is a consequence of the plate-like character of the lithosphere, and that the toroidal part of the velocity field should decrease with depth in the mantle. The strong rheological non-linearity plays the key role for creating mobile plates and to generate the toroidal flow component. While a strong stress dependence acts to localize zones of surface divergence and convergence, it is not clear if it would be sufficient to localize also zones of horizontal simple shear, i.e. lead to the formation of transform faults.

Some other kind of non-Newtonian behaviour may also be required to this end, for example viscous anisotropy or creep mechanisms with memory to the past straining history.

ACKNOWLEDGMENTS

REFERENCES

Bercovici, D., Schubert, G., Glatzmeier, G. A. & Zebib, A., 1989a. Three-dimensional convection in a spherical shell, *J. Fluid Mech.*, **206**, 75–104.

Bercovici, D., Schubert, G. & Glatzmeier, G. A., 1989b. Influence of heating mode on three-dimensional mantle convection, *Geophys. Res. Lett.*, **16**, 617–620.

Bolton, E. & Ribe, N., 1989. Square cell convection in a fluid with temperature-dependence viscosity (abstract), *EOS, Trans. Am. geophys. Un.*, **43**, 1333.

Booker, J. R., 1976. Thermal convection with strongly temperature-dependent viscosity, *J. Fluid Mech.*, **76**, 741–754.

Busse, F. H., 1967. On the stability of two-dimensional convection in a layer heated from below, *J. Math. Phys.*, **46**, 140–150.

Busse, F. H. & Frick, H., 1985. Square-pattern convection in fluids with strongly temperature-dependent viscosity, *J. Fluid Mech.*, **150**, 451–465.

Christensen, U., 1984a. Convection with pressure- and temperature-dependent non-Newtonian rheology, *Geophys. J. R. astr. Soc.*, **77**, 343–384.

Christensen, U., 1984b. Heat transport by variable viscosity convection and implications for the earth's thermal evolution, *Phys. Earth planet. Inter.*, **35**, 264–282.

Christensen, U., 1985. Heat transport by variable viscosity convection II: pressure influence, non-Newtonian rheology, and decaying heat sources, *Phys. Earth planet. Inter.*, **37**, 183–205.

Cserepes, L. & Christensen, U., 1990. Three-dimensional convection under drifting plates. *Geophys. Res. Lett.*, in press.

Cserepes, L., Rabinowicz, M. & Rosenberg-Borot, C., 1988. Three-dimensional infinite Prandtl-number convection in one and two layers and implications for the earth's gravity field, *J. geophys. Res.*, **93**, 12 009–12 025.

Forte, A. M. & Peltier, W. R., 1987. Plate tectonics and aspherical earth structure: The importance of poloidal–toroidal coupling, *J. geophys. Res.*, **92**, 3645–3680.

Frick, H., Busse, F. H. & Clever, R. M., 1983. Steady three-dimensional convection at high Prandtl-number, *J. Fluid Mech.*, **127**, 141–153.

Gable, C. W., O'Connell, R. J. & Travis, B., 1988. Plate motion in models of 3-D convection with layered viscosity: implications for mantle flow (abstract), *EOS, Trans. Am. geophys. Un.*, **69**, 1414.

Haddon, R. A. W. & Buchbinder, G. C. R., 1987. *S*-wave-scattering by 3-D heterogeneities at the base of the mantle, *Geophys. Res. Lett.*, **14**, 891–894.

Hager, B. H. & O'Connell, R. J., 1979. Kinematic models of large-scale flow in the earth's mantle, *J. geophys. Res.*, **84**, 1031–1048.

Houseman, G., 1988. The dependence of convection planform on the mode of heating, *Nature*, **332**, 346–349.

Houseman, G., 1990. The thermal structure of mantle plumes: axisymmetric or triple-junction?, *Geophys. J. Int.*, **102**, 15–24.

Jarvis, G. T. & Mitrovica, J. X., 1989. On Nusselt numbers and relative resolution of plumes and boundary layers in mantle convection, *Geophys. J. Int.*, **99**, 497–510.

Kirby, S. H. & Kronenberg, A. K., 1987. Rheology of the lithosphere: selected topics, in *US National Report to International Union of Geodesy and Geophysics 1983–1986, Contributions in Tectonophysics*, pp. 1219–1244, American Geophysical Union, Washington, DC.

Lapidus, L. & Pinder, C. F., 1982. *Numerical Solution of Partial Differential Equations in Science and Engineering*. J. Wiley, New York.

Loper, D. & Stacey, F. D., 1983. The dynamical and thermal structure of deep mantle plumes, *Phys. Earth planet. Inter.*, **33**, 304–317.

Nataf, H.-C., 1990. Mantle convection, plates, and hotspots, *Tectonophysics*, in press.

Olson, P. & Christensen, U., 1986. Solitary wave propagation in a fluid conduit within a viscous matrix, *J. geophys. Res.*, **91**, 6367–6374.

Parmentier, E. M., Turcotte, D. L. & Torrance, K. E., 1976. Studies of finite amplitude non-Newtonian thermal convection with application to convection in the earth's mantle, *J. geophys. Res.*, **81**, 1839–1846.

Ricard, Y. & Vigny, C., 1989. Mantle dynamics with induced plate tectonics, *J. geophys. Res.*, **94**, 17 543–17 560.

Richter, F. M., Nataf, H.-C. & Daly, S. F., 1983. Heat transfer and horizontally averaged temperature of convection with large viscosity variations. *J. Fluid Mech.*, **129**, 173–192.

Stengel, K. C., Oliver, D. S. & Booker, J. R., 1982. Onset of convection in a variable viscosity fluid, *J. Fluid Mech.*, **120**, 411–431.

Travis, B., Weinstein, S. & Olson, P., 1990. Three-dimensional convection planforms with internal heat generation, *Geophys. Res. Lett.*, **17**, 243–246.

Turcotte, D. L., Torrance, K. E. & Hsui, A. T., 1973. Convection in the earth's mantle, *Meth. comp. Phys.*, **13**, 431–454.

White, D., 1988. The planforms and onset of convection with a temperature-dependent viscosity, *J. Fluid Mech.*, **191**, 247–286.

Whitehead, J. A. & Parsons, B., 1978. Observations of convection at Rayleigh numbers up to 760,000 in a fluid with large Prandtl number, *Geophys. Astrophys. Fluid Dyn.*, **9**, 201–217.